Supporting Information

Schopf et al. 10.1073/pnas.1419241112

SI Methods

Optical Microscopy. For studies by optical microscopy at University of California, Los Angeles (UCLA), uncovered petrographic thin sections were veneered by a thin (~1-μm-thick) layer of fluorescence-free microscopy immersion oil (R. P. Cargille Laboratories). Photomicrographs (Figs. 1, 2 *B–D, F–H*, and *L–R*, and 3 *D–G* and Figs. S2 *A–I, J, M*, and *P* and S4 *A–I* and *K*) were acquired using a Leitz Orthoplan 2 biological microscope (Leica Microsystems) equipped with a Nikon DS-5M-L1 digital microscope camera (Nikon Instruments).

At Universidad de Concepción, Chile, transmitted white light and phase contrast photomicrographs of modern sulfuretum bacteria (Figs. 2 *A* and *I–K* and Fig. 3 *A–C*) were acquired using a trinocular Zeiss A1 Axio Imager microscope (Carl Ziess Inc./ W. Reichman y Cia. Ltda.) equipped with a binocular phototube, Zeiss Plan-Neofluar objectives, and a Canon PowerShot G6 digital camera (W. Reichman y Cia. Ltda.).

Raman Spectroscopy. Raman spectra (Fig. S5) and 2D Raman images (Figs. 2 *S–U* and 3 *H* and *I* and Figs. S2 *K, L, N, O, Q, and R* and S3 *J* and *L–N*) of the fossils and associated minerals were obtained at UCLA by use of a T64000 (JY Horiba) triple-stage laser-Raman system that has macro-Raman and confocal micro-Raman capabilities. This system permitted acquisition both of point spectra and of Raman images that display the 2D spatial distribution of molecular-structural components of the specimens and their associated matrix, with the varying intensities in such images corresponding to the relative concentrations of the molecular structures detected. Due to the confocal capability of this system, use of a 50× objective (having an extended working distance of 10.6 mm and a numerical aperture of 0.5) provided a horizontal resolution of ~1.5 μm and a vertical resolution of 2–3 μm, with use of a 100× objective (working distance: 3.4 mm; numerical aperture: 0.8) providing a horizontal resolution of <1 μm and a vertical resolution of ~1 μm. A Coherent Innova argon ion laser provided excitation at 457.9 nm permitting data to be obtained over a range from ~300 cm^{-1} to ~3,000 cm^{-1} by use of a single spectral window centered at 1,800 cm^{-1}. Thus, Raman spectra could be acquired simultaneously of the major bands (at ~1,350 cm^{-1} and ~1,605 cm^{-1}) of the kerogen comprising the fossils as well as of the major bands of associated minerals: quartz (SiO_2), at ~466 cm^{-1}; pyrite (FeS_2), at ~381 cm^{-1}; and anatase (TiO_2), at ~639 cm^{-1}, ~517 cm^{-1}, and ~396 cm^{-1}.

For Raman imaging, the specimen-containing thin section was covered by a thin veneer of the fluorescence-free microscopy immersion oil noted above (the presence of which has been shown to have no discernable effect on the Raman spectra acquired), and the fossil was centered in the path of the laser beam projected through the microscope of the system. The laser power used was ~1–8 mW over a ~1-μm spot, an instrumental configuration well below the threshold resulting in radiation damage to such specimens (1).

Secondary Ion Mass Spectroscopy.

Sample preparation. Pyritized filamentous microfossils and associated pyrite were located and photographed in two polished ~100-μm-thick thin sections of Duck Creek chert (M.R.W. collection 12.06.18.2, compare PPRG samples 049–053; Fig. S1). Two grains of the University of Wisconsin SIMS pyrite standard UWPy-1 [$\delta^{34}S_{(VCDT)}$ = 16.04‰; Dataset S1] were face-mounted into each thin section near the center of an area containing targets selected for sulfur isotope analysis. Using a low-speed water-cooled diamond saw (Buehler IsoMet), each thin section was cut and ground into a 2.54-cm-diameter disk with the standard grains at their center. Newly developed large sample holders (2) that provide high precision and accuracy for targets within 8 mm (in comparison with 5 mm for standard sample holders) of the center of the discs were used, and all measurements were performed within this area. Before analyses, the discs were cleaned by sonicating sequentially three times each for 1 min in deionized water, for 30 s in ethanol, and twice, each for 30 s, in deionized water, and immediately dried under a stream of high-purity nitrogen.

The pyritic specimens to be analyzed were then photomicrographed in combined transmitted and reflected light (*Insets* in Fig. 4 *A–C*). A thin (~5 nm) gold coat was applied to the mounts, and scanning electron microscope images were acquired in backscattered electron mode to document the distribution of pyrite exposed at the surface in the areas to be analyzed. A thicker (~30 nm) gold coat was then applied to facilitate charge compensation during SIMS analysis, the samples were degassed for 48 h at 10^{-9} torr in the SIMS air-lock sample chamber before analysis, analyses were performed, and scanning electron micrographs were again acquired (Fig. 4).

Sulfur isotope analysis. Isotopic analyses were performed using the WiscSIMS CAMECA IMS-1280 (CAMECA SAS) in the Department of Geoscience, University of Wisconsin–Madison. For relatively large targets, a $^{133}Cs^+$ primary ion beam with an intensity of 150 pA was focused into an ellipse of 10-μm maximum dimension at the sample surface. For smaller targets, a primary beam intensity of 30 pA with a beam-spot size of 5 μm was used. Secondary ion accelerating voltage was 10 kV. $^{30}Si^-$, $^{32}S^-$, and $^{34}S^-$ were simultaneously collected using detector L2 (electron multiplier) for $^{30}Si^-$ and L1 and H2 (Faraday cups) for $^{32}S^-$ and $^{34}S^-$, respectively. Mass resolving power (M/ΔM at 10% peak height) was ~2,200. Presputtering time was 10 s, followed by an automatic centering of the secondary ion beam in the field aperture and counting of the secondary ions (20 cycles of 4 s each). The majority of the 10-μm beam was concentrated into an ellipse having a maximum diameter of ~4 μm; for the 5-μm beam, an ellipse of <2 μm. This nonstandard tuning method effectively increased spatial resolution of analyses (see pit images in Fig. 4 and Fig. S2) and produced no degradation of precision or accuracy in the bracketing pyrite standard measurements made using the same analytical conditions (Fig. S2 and Dataset S1).

Analytical precision. Four to seven consecutive measurements of UWPy-1 were performed before and after each set of 5–15 sample analyses. Using a ~10-μm-beam, the average spot-to-spot reproducibility of the standard was 0.28‰ (2 SD). For use of the 5-μm beam, external precision was 0.76‰ (2 SD), a relatively lower analytical reproducibility due to its lower ion count rates of small samples where the SIMS pit overlapped the chert matrix.

Analytical results. A total of 118 measurements were made: 52 of the UWPy standard, 30 of pyritized filaments, and 36 of associated pyrite (Dataset S1). Using a ~10-μm-diameter spot, $\delta^{34}S_{(VCDT)}$ ranged from –9.4‰ to 37.4‰; for use of a ~5-μm-diameter spot, from 4.6‰ to 43.4‰.

Interpretation of SIMS-Determined $\delta^{34}S_{(VCDT)}$ Values. Previous analyses of $\delta^{34}S$ values for carbonate-associated pyrite in rocks of similar age to the ~1.8-Ga-old Duck Creek fossiliferous cherts include those of Lyons et al. (3) and Gellatly and Lyons (4) from the ~1.65-Ga Paradise Creek Formation—recording maximum

δ^{34}S values of ~40‰, like those reported here—whereas one earlier (1992) study of Duck Creek pyrite reported a δ^{34} value of 17.0‰ (5). In rocks older than the ~1.8-Ga Duck Creek Formation, the sulfate δ^{34}S record is patchy, known only from massive sulfates (6).

Evidently, the highly positive δ^{34}S pyrite values reported here for ~1.8-Ga Duck Creek pyrite provide the earliest known sulfur isotopic evidence of a postulated increase in δ^{34}S seawater sulfate between ~1.9 Ga and ~1.65 Ga that may record an O_2-dependent (GOE-resultant) transition in the Paleoproterozoic marine environment, an interpretation consistent with iron speciation

measurements on the similarly aged Gunflint and Rove Formations of southern Canada (7).

Were evidence to show that the δ^{34}S of seawater sulfate in the Duck Creek basin was lower than the maximum values of pyrite reported here (~40‰), such data would suggest that the isotopically anomalous sulfide here measured would likely have required that sulfide oxidizers produced isotopically relatively light SO_4, driving the residual H_2S toward higher isotopic values that resulted in pyrite having a δ^{34}S value higher than seawater sulfate, as has been inferred for pyrite of the Neoproterozoic Nama Group of southern Africa (8).

1. Schopf JW, Kudryavtsev AB, Agresti DG, Czaja AD, Wdowiak TJ (2005) Raman imagery: A new approach to assess the geochemical maturity and biogenicity of permineralized precambrian fossils. *Astrobiology* 5(3):333–371.
2. Peres P, et al. (2012) New sample holder geometry for high precision isotope analyses. *Surf Interface Anal* 45:553–556.
3. Lyons TW, et al. (2004) Sites of anomalous organic remineralization in the carbonate sediments of South Florida, U.S.A.: The sulfur cycle and carbonate-associated sulfate. *Spec Pap Geol Soc Am* 379:161–176.
4. Gellatly AM, Lyons TW (2005) Trace sulfate in mid-Proterozoic carbonates and the sulfur isotope record of biospheric evolution. *Geochim Cosmochim Acta* 69:3813–3829.
5. Bottomly DJ, et al. (1992) Isotopic composition of disseminated pyrite sulfur in Precambrian sedimentary rocks. *Geochim Cosmochim Acta* 56:3311–3322.
6. Strauss H (2004) 4 Ga of seawater evolution: Evidence from the sulfur isotopic composition of sulfate. *Spec Pap Geol Soc Am* 379:195–205.
7. Poulton SW, Fralick PW, Canfield DE (2004) The transition to a sulphidic ocean approximately 1.84 billion years ago. *Nature* 431(7005):173–177.
8. Ries JB, et al. (2009) Superheavy pyrite ($\delta^{34}S_{pyr} > \delta^{34}S_{CAS}$) in the terminal Proterozoic Nama Group, southern Namibia: A consequence of low seawater sulfate at the dawn of animal life. *Geology* 37:743–746.
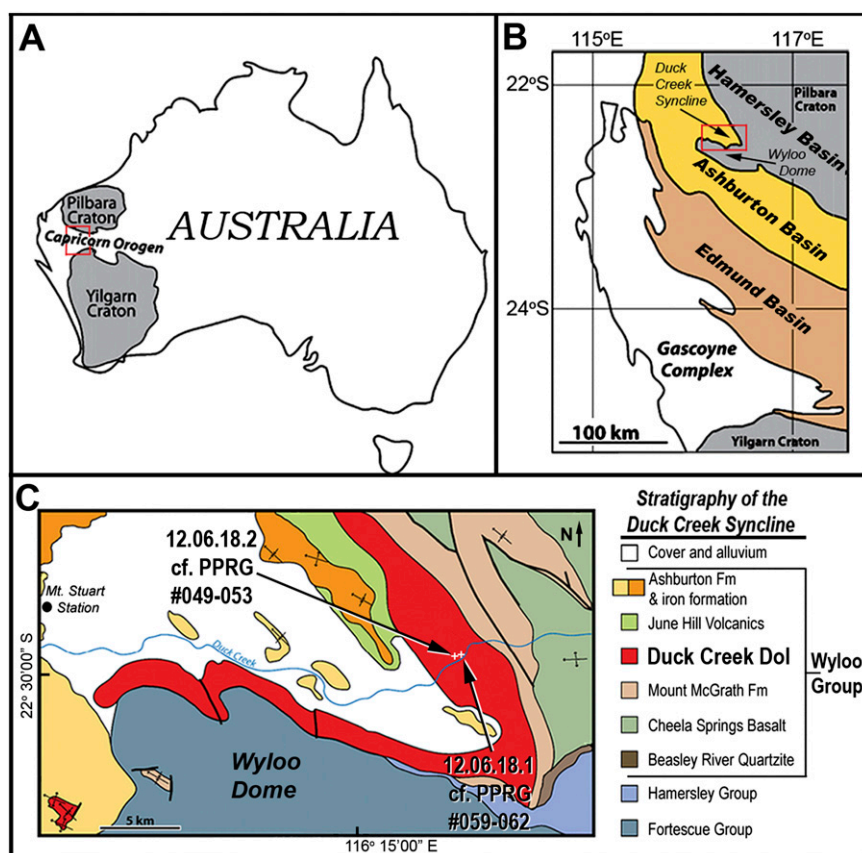
**Fig. S1.** Maps showing the location of the fossiliferous Duck Creek localities. Reprinted from ref. 1 with permission from Elsevier; www.sciencedirect.com/science/journal/03019268. (*A*) Tectonic sketch map of Western Australia showing the location of the Duck Creek strata in the Capricorn Orogen. (*B*) Map showing the location of the sedimentary basins of the Capricorn Orogen and the Duck Creek Syncline. (*C*) Geologic map showing the location in the Duck Creek Syncline of fossiliferous cherts of the ~1.8-Ga Duck Creek Formation studied here (M.R.W. collection 12.06.18.1, compare PPRG samples 059–062, latitude 22.29.213°S, longitude 116.18.986°E; and 12.06.18.2, compare PPRG samples 049–053, lat. 22.29.208°S, long. 116.18.886°E). Fossil-bearing cherts of the ~500-Ma-older Turee Creek Group Kazput Formation (Figs. 1 *D–F*, 2 *B* and *L–N*, and 3*D*), recently reported (2) to contain a microbial assemblage essentially identical to that of the fossiliferous Duck Creek chert, occur ~65 km to the southeast (lat. 22.48°S, long. 116.52°E).

1. Wilson JP, et al. (2010) Geobiology of the late Paleoproterozic Duck Creek Formation, Western Australia. *Precambrian Res* 179:135–149.
2. Grice K, et al. (2012) A 2.3 Ga sulfuretum at the GOE: Microfossils and organic geochemistry evidence from the Turee Creek Group, Western Australia. *Astrobiology Science Conference 2012* (NASA Astrobiol Program, Atlanta, GA), Abstract 2084. Available at abscicon2012.arc.nasa.gov/abstracts.
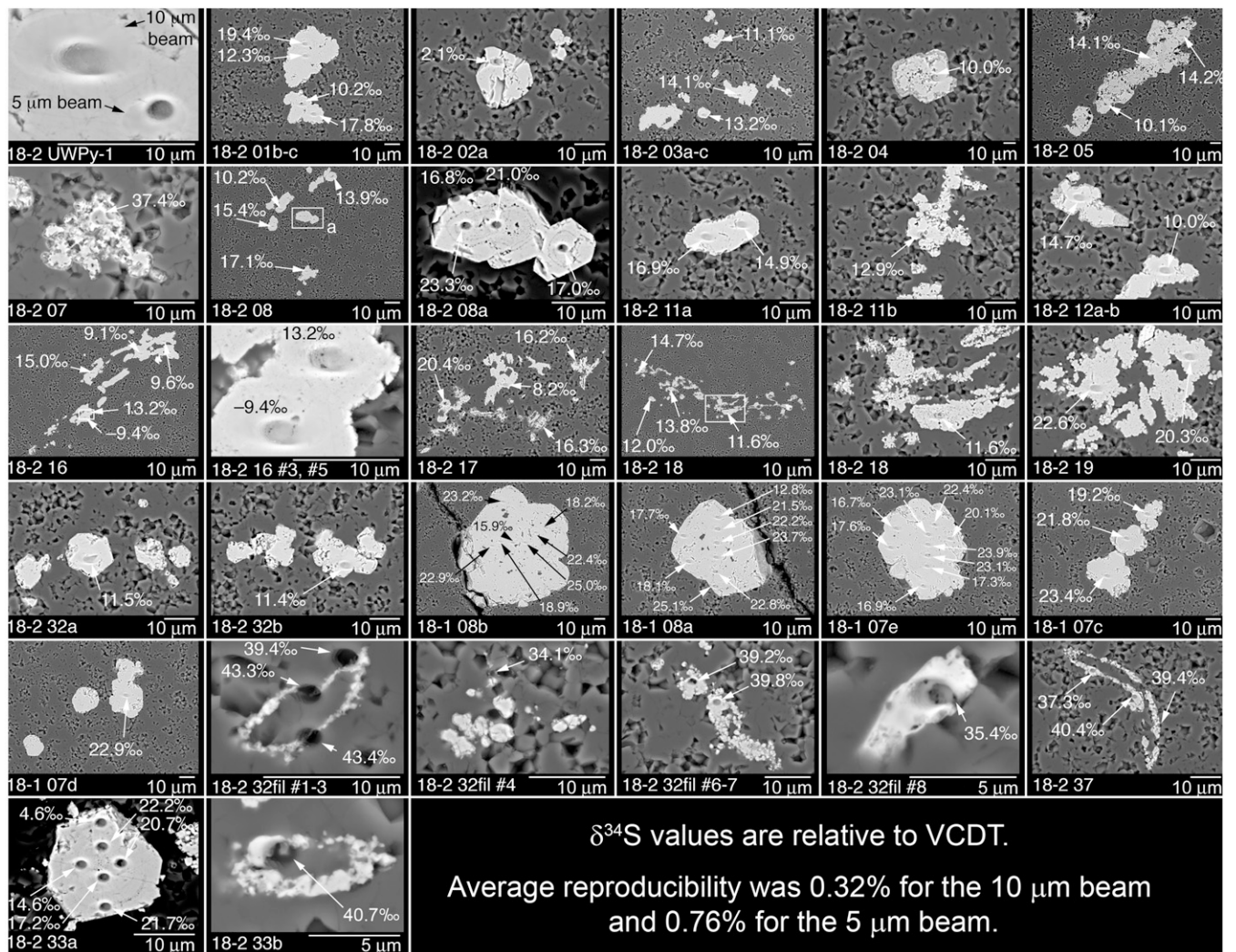
Fig. S2. Target and analytical pit images showing WiscSIMS $\delta^{34}S$ measurements of the UWPy-1 standard and pyritized microfossil filaments and associated pyrite from the ~1.8-Ga Duck Creek Formation. Targets are shown roughly in order of acquisition (Dataset S1). *Top Left* shows single analytical pits produced by the SIMS ~10-μm and ~5-μm beam spots (see *SI Methods*). The $\delta^{34}S$ values are indicated in ‰ VCDT with the corresponding analytical pits indicated by arrows.
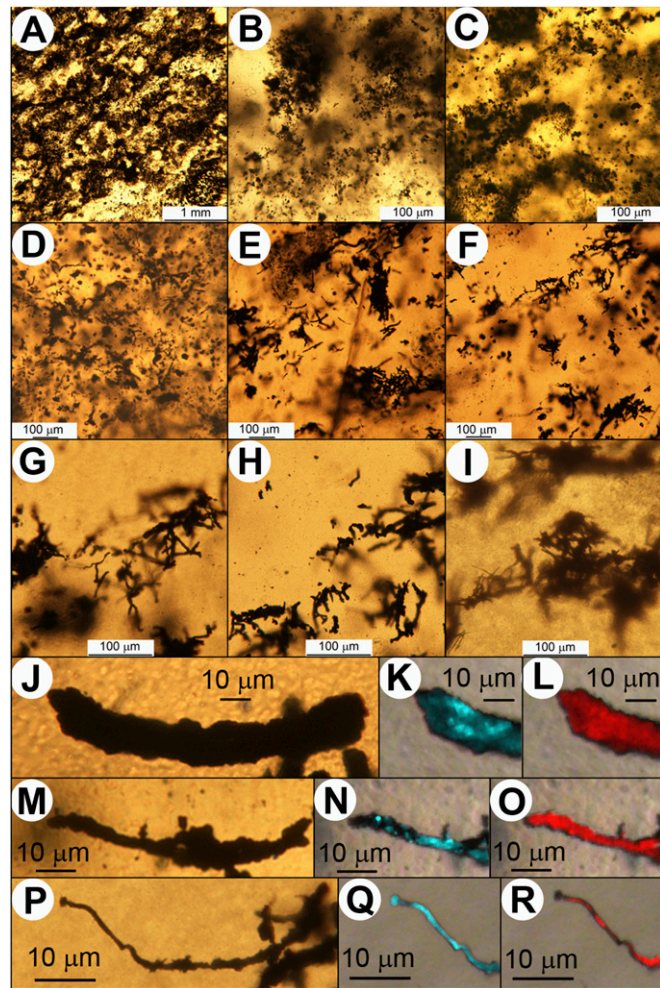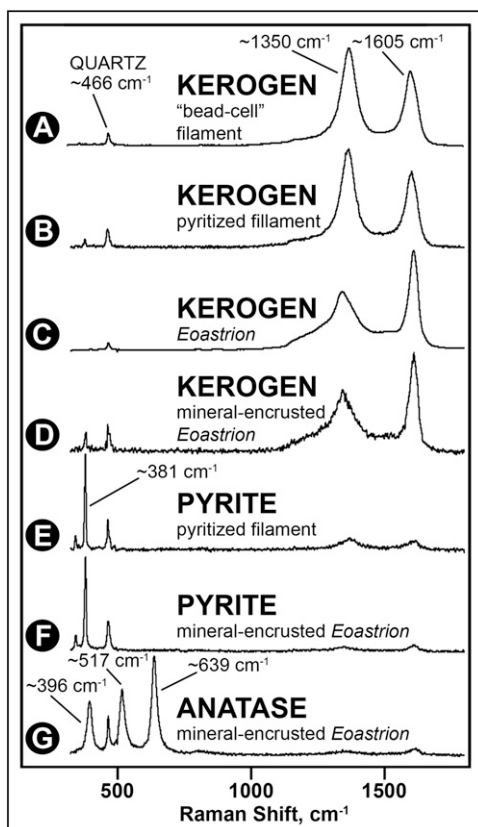
Fig. S3. Pyrite and pyritized filamentous fossils of the Duck Creek chert (PPRG samples 049−051). (*A*) Pyrite-rich fabric. (*B* and *C*) Pyrite granules. (*D*) Pyrite granules and pyritized microbial filaments. (*E*−*R*) Pyritized filaments. (*J*−*R*) Higher magnification photomicrographs of representative pyritized filaments (*J*, *M*, and *P*) and accompanying Raman images of the ends of these optically imaged filaments that document their carbonaceous composition (*K*, *N*, and *Q*; blue) and secondarily emplaced pyrite (*L*, *O*, and *R*; red), established by Raman spectra (Fig. S4).
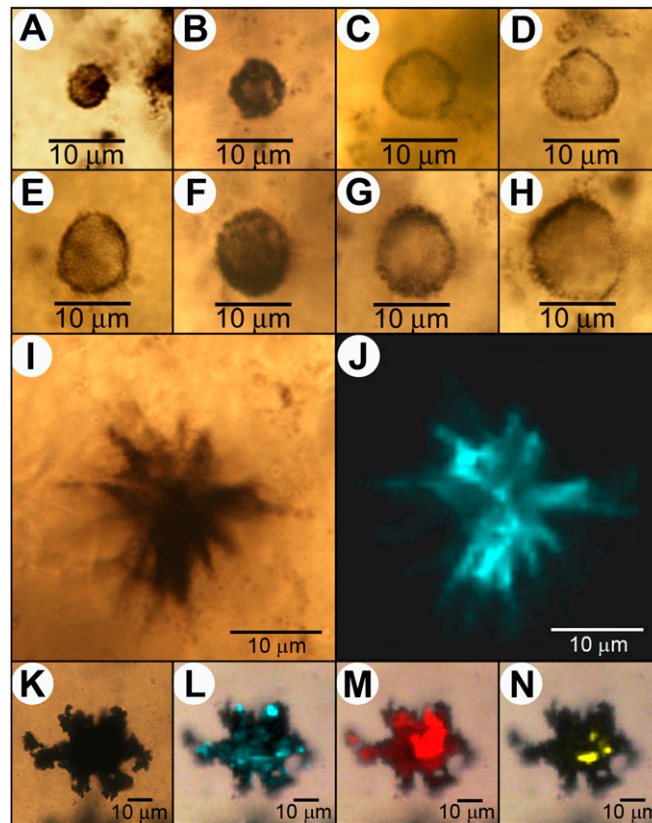
Fig. S4. Nonfilamentous microfossils of the Duck Creek chert. *Huroniospora*-like unicells (*A*−*H*; PPRG sample 062), compare modern *Thiovulum* (1) and kerogenous (*I* and *J*) and mineral-encrusted (*K*−*N*) specimens of the asteriform microbe *Eoastrion* (PPRG sample 062), compare modern *Metallogenium*. As shown by Raman images (*J* and *L*−*N*) and Raman spectra (Fig. S4), the dark brown unmineralized specimen of *Eoastrion* (*I*) is composed of kerogen (*J*, blue) whereas the optically opaque mineralized specimen (*K*) is composed of kerogen (*L*, blue) encrusted by pyrite, FeS_2 (*M*, red), presumably a replacement of originally precipitated manganese and/or iron oxides, and small concentrations of anatase, TiO_2 (*N*, yellow), a minor constituent of the minerals encrusting modern *Metallogenium* (2).

1. Muir MD (1974) Microfossils from the Middle Precambrian McArthur Group, Northern Territory, Australia. *Orig Life* 5(1):105–118.
2. Garcia-Pichel F (1989) Rapid bacterial swimming measured in swarming cells of *Thiovulum majus*. *J Bacteriol* 171(6):3560–3563.

Fig. S5. Raman spectra of Duck Creek microbial fossils and associated minerals. Kerogen spectra of (*A*) a carbonaceous bead-cell filamentous microbe (Fig. 2*R*); (*B*) a pyritized filament (Fig. S2*Q*); (*C*) a carbonaceous specimen of *Eoastrion* (Fig. S3*J*); and (*D*) a mineral-encrusted specimen of *Eoastrion* (Fig. S3*L*). Pyrite spectra of (*E*) a pyritized filament (Fig. S2*R*) and (*F*) a pyrite-encrusted specimen of *Eoastrion* (Fig. S3*M*). (*G*) Spectrum of anatase encrusting an *Eoastrion* specimen (Fig. S3*N*).

Other Supporting Information Files

Dataset S1 (XLS)